Universiteit
Leiden
The Netherlands

The evolving velocity field around protostars

Brinch, C.

Citation
Brinch, C. (2008, October 22). *The evolving velocity field around protostars*. Retrieved from https://hdl.handle.net/1887/13155

Version:	Corrected Publisher's Version
License:	Licence agreement concerning inclusion of doctoral thesis in the Institutional Repository of the University of Leiden
Downloaded from:	https://hdl.handle.net/1887/13155

Note: To cite this publication please use the final published version (if applicable).

Chapter 6

The kinematics of NGC1333-IRAS2A – a true Class 0 protostar

Abstract

Low-mass star formation is described by gravitational collapse of dense cores of gas and dust. At some point during the collapse, a disk is formed around the protostar and the disk will spin up and grow in size as the core contracts because of angular momentum conservation. The question is how early in the process the disk formation occurs. In this chapter we aim to characterize the kinematical state of a deeply embedded, Class 0 young stellar object, NGC1333–IRAS2A, based on high resolution interferometric observations of HCN and $H^{13}CN$ J = 4–3 from the Submillimeter Array, and test whether a circumstellar disk can be detected based on gas kinematic features. We adopt a physical and chemical model which has been shown to describe the object well and obtain a fit of a parameterized model of the velocity field, using a two-dimensional radiation transfer code. The parameterization and fit to the high resolution data make it possible to characterize the central dynamical mass and the ratio of infall velocity to rotation velocity. We find a large amount of infall and very little rotation on all scales. The central object has a relatively low mass of 0.25 $M_\odot$. Our best fit is consistent with both the interferometer data and single-dish observations of the same molecule. As a Class 0 object with a low stellar mass compared to the envelope mass, we conclude that NGC1333–IRAS2A is consistent with the theoretical prediction that Class 0 objects represent the very earliest stages of star formation. The large amount of infall relative to rotation also suggests that this is a young object. We do however find the need of a central compact component on scales < 100 AU based on the continuum data, which suggests that disk formation happens very shortly after the initial gravitational collapse. The data do not reveal a distinct velocity field for this 0.1 $M_\odot$ component.

Christian Brinch, Jes K. Jørgensen, and Michiel R. Hogerheijde

Submitted to Astronomy & Astrophysics

6.1 Introduction

An open question in the subject of low-mass star formation is how and when the velocity field of the molecular gas in the protostellar envelope changes from being dominated by radial infall to being dominated by Keplerian rotation. It is well known that in the early stages of star formation, gas falls toward the center as gravitational collapse sets in (Shu 1977). Cores, however, are known to carry a certain amount of rotational energy (Goodman et al. 1993), so as a core contracts, the net angular momentum spins it up, flattening the infalling material in the direction of the rotation axis (Cassen & Moosman 1981; Terebey et al. 1984; Adams et al. 1988; Basu 1998). After the main accretion phase, the envelope is gone and a planet forming disk with gas in Keplerian orbits is left. In chapter 3 we showed that the evolution of the velocity field, from the collapse phase to the disk phase, can be described by a single parameter, namely the radially averaged ratio of infall to rotation, which may be linked to the age of the protostar and can thus tell us about the evolutionary stage of the system.

Currently, the most widespread way to classify young stellar objects is through the classification scheme laid out by Lada & Wilking (1984) with the addition of the Class 0 by André et al. (1993). These classes are based on the shape of the spectral energy distribution with the addition that Class 0 objects are defined as protostars with $M_* < M_{\rm env}$, which is equivalent to the original empirical definition of Class 0 objects as stars with a high submillimeter flux relative to their bolometric luminosity. Furthermore, for Class 0 objects, the mass of disks is usually thought to be much less than the mass of the envelope. The mass of the central object is not easily measured, but one way to estimate it is by determining the velocity field, since the magnitude of the velocity vectors are determined by the central mass. In this chapter, we study the kinematics of the deeply embedded NGC1333-IRAS2A protostar using subarcsecond resolution data from the Submillimeter Array (SMA) as well as detailed two-dimensional line radiative transfer modeling.

NGC1333-IRAS2 was first detected through IRAS observations by Jennings et al. (1987). Submillimeter continuum imaging has subsequently shown that it likely consists of three different objects, NGC1333-IRAS2A, -IRAS2B, and -IRAS2C, of which the two former are well isolated and detected at mid-IR wavelengths, e.g., with the Spitzer Space Telescope (Jørgensen et al. 2007b; Gutermuth et al. 2008). These sources also show compact emission in millimeter interferometric images (Looney et al. 2000; Jørgensen et al. 2004b). The third source, IRAS2C, shows relatively strong N_2H^+ emission possibly reflecting the absence of a central heating source (Jørgensen et al. 2004b). Modeling of the high angu-

lar resolution millimeter continuum observations (Looney et al. 2003; Jørgensen et al. 2004b) revealed the existence of a central compact continuum component in NGC1333-IRAS2A, likely reflecting the presence of a central circumstellar disk with a mass of $\sim 0.1\ M_{\odot}$ (depending on the assumed dust temperature and opacity). NGC1333-IRAS2A was targeted as part of the PROSAC survey of Class 0 embedded protostars (Jørgensen et al. 2005b, 2007a). The $1''$ resolution submillimeter continuum data (Jørgensen et al. 2005b) showed that the central compact component was resolved with a diameter of approximately 300 AU.

In this chapter we investigate the kinematical properties of IRAS2A using a global parameterization of the velocity field. We are particularly interested in the velocity structure on scales <100 AU, traced by the high resolution Submillimeter Array[1] data, where a circumstellar disk is thought to be present. The SMA instrument is ideal for this task because we can probe the warm, dense gas with high excitation lines in high resolution and thereby zoom in on the central parts of the object. We furthermore benefit from the fact that the interferometer is less sensitive to ambient cloud material.

6.2 Observations

Supplementing the SMA compact configuration data from 2004 October 17 (Jørgensen et al. 2005b), NGC1333-IRAS2A was observed in the extended configuration on 2006 January 8. The weather was good and stable during the observations with a sky opacity at 225 GHz of about 0.05. Seven of the eight SMA antennas were in the array at the time which together with the 2004 compact configuration data provide good (u, v)-coverage on baselines between 17 and 210 kλ with a few baselines at 232 to 264 kλ. The complex gains were calibrated by observations of the strong quasars 3c84 (2.2 Jy) and 3c111 (2.8 Jy) every 15 minutes.

The SMA correlator was configured with an identical setup to the compact configuration data from 2005 with 2 GHz bandwidth at 345 GHz (LSB) and 355 GHz (USB). For the lines predominantly discussed in this chapter, HCN and $H^{13}CN$ J= 4–3 at respectively 354.5055 and 343.3398 GHz, the spectral resolution was 0.15 km s^{-1} (HCN) and 0.30 km s^{-1} ($H^{13}CN$). With natural weighting the RMS is 0.225 (HCN) and 0.147 ($H^{13}CN$) Jy beam^{-1} in a 1 km s^{-1} wide channel with a beam size of $1.2'' \times 0.8''$. The initial calibration of the data was done with the SMA MIR package (Qi 2006) with additional image processing done using

[1]The Submillimeter Array is a joint project between the Smithsonian Astrophysical Observatory and the Academia Sinica Institute of Astronomy and Astrophysics and is funded by the Smithsonian Institution and the Academia Sinica.

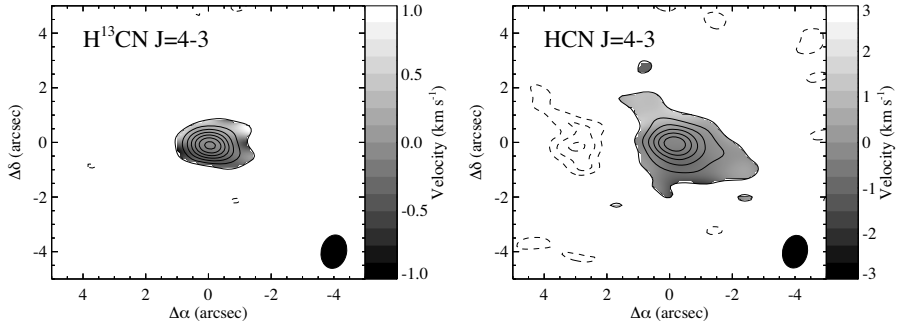

Figure 6.1: Zero (contours) and first (gray scale) moments of $H^{13}CN$ and HCN $J = 4$–3. Contour lines showing the integrated intensity begin at 3σ and increase by 3σ=2.3 Jy km s^{-1} ($H^{13}CN$) and 5.4 Jy km s^{-1} (HCN), respectively.

MIRIAD (Sault et al. 1995).

In addition to these data, we here use previously published single-dish data from the James Clerk Maxwell Telescope (Jørgensen et al. 2004b) as well as 3 mm interferometric observations from the BIMA array (Jørgensen et al. 2004a).

6.3 Results

The data have been inverted in order to reconstruct the emission distribution in the image plane, using the *invert, clean,* and *restore* routines of the MIRIAD software package. We use the natural weighting scheme during the *invert* procedure to optimize for signal-to-noise in the resulting image at a small cost of resolution. The zeroth and first moments of the image cubes, integrated intensity and velocity, respectively, have been plotted in Fig. 6.1 for both the $H^{13}CN$ line and HCN line. In this figure, the contour lines show the zeroth moment and the grey scale shows the first moment. The contours start at the three sigma level corresponding to 5.5 Jy beam^{-1} for HCN and 2.5 Jy beam^{-1} for $H^{13}CN$ and they increase linearly by three sigma in both panels. The emission is seen to be centrally peaked with only a bit of extended emission at the 3–6 σ level in HCN. This is in good agreement with the (u, v)-amplitude plots in Fig. 6.2 where HCN is seen to be resolved while $H^{13}CN$ is more compact.

When the two SMA tracks are combined we get a good (u, v)-coverage on

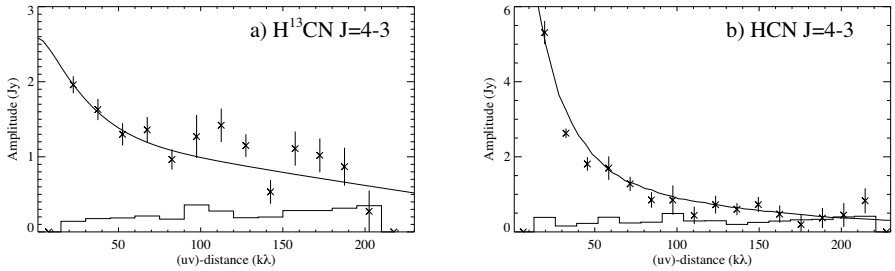

Figure 6.2: Averaged (u, v)-amplitudes over the velocity range of ±3 km s^{-1} from the systemic velocity of H^{13}CN and HCN. The histogram is the expected amplitude if no signal was present. The solid line is our best fit model as discussed in Sect. 6.4.

baselines between 17 and 210 kλ. This is equivalent to emission on scales of 1.2″ to 14.8″ which, at the distance of NGC1333 (220 pc; Cernis 1990), corresponds to linear scales of 264 to 3300 AU. Some flux is also measured on scales between 232 and 264 kλ (216 to 238 AU), but at low signal-to-noise. Any emission on baselines shorter than 17 kλ is filtered out by the interferometer. Figure 6.2 shows the averaged (u, v)-amplitudes as a function of baseline between 0 and 210 kλ. In panel a) is shown the H^{13}CN $J = 4$–3 line. This panel shows that the emission on all scales up to 200 kλ is compact with only a hint of increased flux on scales below 50 kλ. The histogram indicates the expectation values if no signal were present and the full line is our best fit model, which we discuss in Sect. 6.4. Panel b) has a similar layout, but for the HCN $J = 4$–3 line. This emission is well resolved on scales below 80 kλ, but less resolved on scales above this distance. It is, however, clearly detected on all baselines with an almost constant signal-to-noise, even on the longest baselines.

Figure 6.3 show the three position-velocity (PV) diagrams of both H^{13}CN and HCN. The PV-diagrams show the emission contours along one spatial axis and a range in velocities. The three panels of Fig. 6.3 correspond to PV-diagrams along slices of different position angles. If a rotation axis is present, the PV-diagram along this axis should show no sign of rotation, whereas the PV-diagram along the perpendicular axis should. The three axes for which we show PV-diagrams are chosen so that one coincides with the direction of the velocity gradient seen in Fig. 6.1 (the same direction as the north-south outflow), one which is perpendicular to the previous one (coinciding with the east-west outflow), and one which is

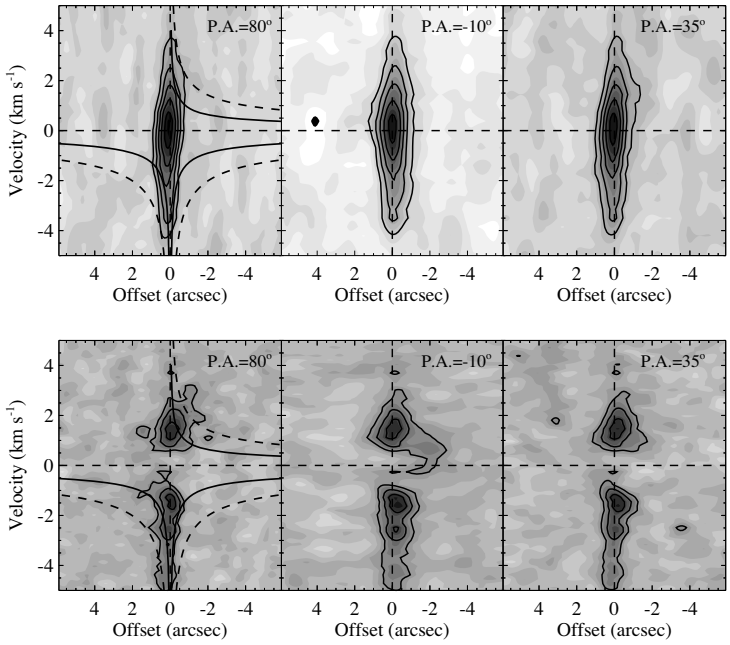

Figure 6.3: PV-diagrams of the combined SMA data sets of $H^{13}CN$ J =4–3 and HCN J =4–3. The three panels correspond to slices along different position angle with PA=80° being the direction of the north-south outflow, PA=-10° the direction of the east-west outflow, and PA=35° the direction which lines up IRAS2B and IRAS2C. The PV-diagrams show little difference with changing position angle suggesting no preferred axis of rotation. In the leftmost panels are shown Keplerian rotation (top quadrants) and free-fall (bottom quadrants) profiles for M_*=0.3 $M_\odot$ (full line) and 1.0 $M_\odot$ (dashed line).

inclined with 45° with respect to the other two axis (coinciding with the direction toward IRAS2B and IRAS2C).

The first thing to notice is that the three panels are not very different from each other. There is no obvious rotation axis and with both peak intensities located exactly at zero off-set in all three panels, there is actually very little sign of the velocity gradient at all, except for small skew in the contours in the left-most panel of $H^{13}CN$ and a bit of 3-6 σ emission at positive velocities in the center HCN panel. The black lines that are also plotted in Fig. 6.3 show Keplerian rotation profiles for a central mass of 0.3 $M_\odot$ (full line) and 1.0 $M_\odot$ (dashed line) in the first

quadrant. The curves in the two lower quadrants show free-fall velocity profiles for the corresponding central masses. Obviously, it is not possible to discriminate between rotation and infall by comparing the emission to these curves, because the emission is very compact, even for HCN. The emission contours are, however, more consistent with the 0.3 $M_\odot$ curves than with the 1.0 $M_\odot$ curves. The second thing to notice in the PV-diagrams is how fast the emission drops off along the spatial axis while the emission at small off-sets shows very broad lines. This is true for both HCN and $H^{13}CN$. It is therefore likely that the velocity gradient which is seen in the moment maps is due to the outflow rather than rotation. After all, this gradient does lie in the same direction as the outflow. These PV-diagrams also resemble the ones presented by Hogerheijde et al. (1998) for a number of known outflow sources.

6.4 Analysis

We describe the observed emission with the model for the density and temperature from Jørgensen et al. (2002), who derived this model from analysis of the continuum image of the source at 450 μm and 850 μm as well as at its broadband SED from 60 μm to 1.3 mm. The density is described by a power-law,

$$n(r) = 1.5 \times 10^6 \text{ cm}^{-3} (r/1000 \text{ AU})^{-1.8}, \tag{6.1}$$

while the temperature was calculated using a 1D continuum radiation transfer code as described by Jørgensen et al. (2002, see also Fig. 1f of Jørgensen et al. 2004a). The outer radius of the model is 1.2×10^4 AU. Jørgensen et al. (2004b) also modeled the chemical abundance profiles using the integrated intensity of the optically thin $H^{13}CN$ single-dish lines. They found that to reproduce the line ratios, a model with a depletion zone is needed. The resulting HCN abundance profile reads,

$$X(\text{HCN}) = \begin{cases} 2 \times 10^{-8} & , n_{\text{H}_2} < 7 \times 10^4 \text{ cm}^{-3} \\ 2 \times 10^{-9} & , n_{\text{H}_2} > 7 \times 10^4 \text{ cm}^{-3} \end{cases}, \tag{6.2}$$

assuming an isotopic abundance ratio of $^{12}C/^{13}C = 70$. We furthermore add a central compact component, in accordance to Jørgensen et al. (2005a) who found a need for an abundance increase near the center. We describe this component with a jump in the abundance within the radius above 90 K (~100 AU) to $X(\text{HCN}) = 7 \times 10^{-8}$.

The new addition to the model is a parameterization of the velocity field, which allows for both infall and rotation. This breaks the spherical symmetry

of the model, making it two-dimensional, although we keep the spherical description of the density and temperature. We follow the approach presented in Chapter 3 with a velocity field parameterized by two parameters,

$$\mathbf{v} = \begin{pmatrix} v_r \\ v_\phi \end{pmatrix} = \sqrt{\frac{GM_*}{r}} \begin{pmatrix} -\sqrt{2}\sin\alpha \\ \cos\alpha \end{pmatrix}, \tag{6.3}$$

with M_*, the mass of the central object, and the angle α as free parameter. The velocity parameterization is such that $\alpha = 0$ corresponds to Keplerian rotation and no infall, whereas $\alpha = \pi/2$ corresponds to free fall toward the center and no rotation. The use of this two-dimensional velocity field further introduces two free parameters, namely the inclination of the rotation axis with respect to the plane of the sky and the position angle of the rotation axis in the plane of the sky. We add a mean turbulent velocity field of 0.2 km s^{-1} to the model. While this parameter is somewhat degenerate with the central mass in the sense that it affects the line widths, it cannot account for the different line widths at different resolution. Only by letting the turbulent field vary across the model could we reproduce this effect. We have however chosen to use a constant turbulent field to keep the model simple, and a small change in its value does not affect our result significantly. For an in-depth discussion of turbulent line broadening we refer the reader to, e.g., Ward-Thompson & Buckley (2001).

We use the molecular excitation and radiation transfer code *RATRAN* (Hogerheijde & van der Tak 2000) to determine the level populations of the HCN molecule on a computational domain consisting of multiple nested regular grids. The grid resolves scales from 6 AU to 1.2×10^4 AU, which is about the highest dynamical range of scales we can resolve with *RATRAN* without loosing the gain of the accelerated lambda iteration (ALI) algorithm which makes the code feasible to run on a standard desktop computer. The resulting image cubes are afterward either convolved with the appropriate beam profiles for comparison to the single-dish lines or Fourier transformed for direct comparison to the visibility tables in the BIMA and SMA data sets.

6.4.1 Model fit

We run a grid of models in the parameter ranges $M_* \in \{0.0, 1.0\}$ and $\alpha \in \{0, \pi/2\}$ and we compare the single-dish spectra and PV-diagrams from the SMA data of H^{13}CN only. A χ^2-surface plot is shown in Fig. 6.4 for an inclination of 40°. We add the χ^2 value of the two single-dish transitions, calculated channel by channel on a velocity range from -4 to +4 km s^{-1}, to the χ^2 value of the PV-diagram, where

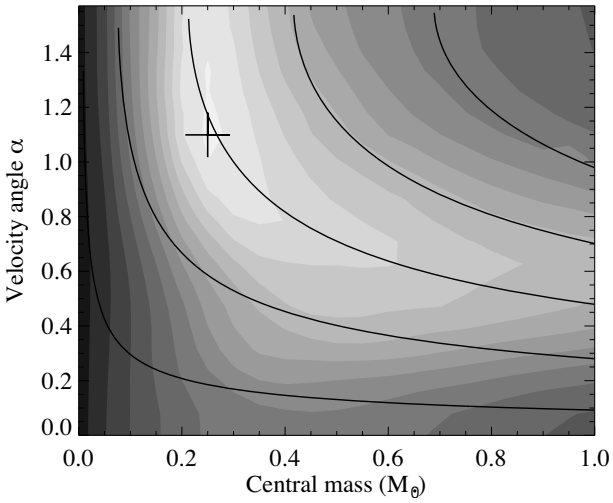

Figure 6.4: $H^{13}CN$ χ^2 surface in the parameters M_* and α. The cross marks the minimum which lies at M_*=0.25 $M_\odot$ and α=1.10 with a χ^2 value of 3.71. The black lines are lines of constant accretion rate, with lines corresponding to 1, 3, 5, 7, and 9 $\times 10^{-5}$ $M_\odot$ yr^{-1} going from the lowest line and up.

we compare pixels with a signal-to-noise better than three only. The χ^2 is seen to be minimized for parameter values of $M_* = 0.25$ $M_\odot$ and $\alpha = 1.10$, which we take to be our best fit model. We have chosen to adopt an inclination parameter value of 40°, because this parameter is not well-constrained by our fit. For any value below $40^c irc$, we get an almost constant χ^2 value and only for values higher than 40° we see a systematic increase in the χ^2. The reason is that our best fit already favors an infall dominated model (i.e., almost spherical velocity field) and therefore the velocity field is mostly independent of the inclination. As we go toward models with more rotation, the fit rapidly deteriorates with increasing inclination, which only support the result that little rotation is present in IRAS2A. Similarly, the position angle is unconstrained for the same reasons, in full agreement with the PV-diagrams shown in Sect. 6.3. We have also plotted lines of constant mass accretion rate in Fig. 6.4. The accretion rate is calculated as

$$\dot{M} = 4\pi r_0^2 \rho_0 \sqrt{\frac{2GM_*}{r_0}} \sin(\alpha) \tag{6.4}$$

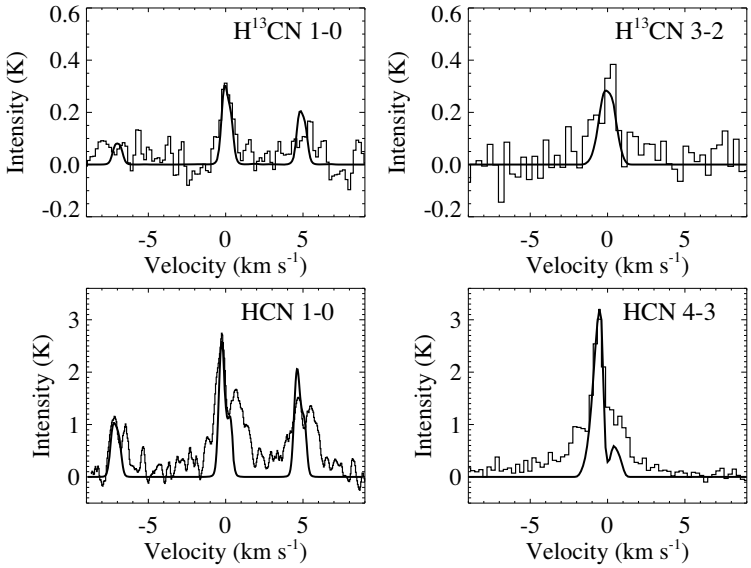

Figure 6.5: Best model fit to the four single-dish transitions of HCN and $H^{13}CN$.

where ρ_0 is the mass density at the distance r_0. Our fit is seen to be consistent with a mass accretion rate of 5×10^{-5} $M_\odot$ yr^{-1}.

The first fit, shown in Fig. 6.5, is that of the single-dish lines $H^{13}CN$ J =1–0, 3–2 and HCN J =1–0, 4–3. Being optically thin, the $H^{13}CN$ lines are quite sensitive to the abundance profile and they constrain the radial variations well, as discussed by Jørgensen et al. (2005a). The single-dish lines fit well, and our best fit model automatically reproduces the (u, v)-amplitudes as well (Fig. 6.2, panel a). The J =1–0 lines show distinct hyperfine components. We model these components under the assumtion of LTE between the hyperfine levels. The hyperfine line ratios are also well reproduced. The HCN lines have a much more distinct profile and they are much more sensitive to the velocity parameters. However, the large optical thickness of HCN and the possible contamination of outflow emission in these lines make it difficult to assess the quality of our model (not the fit) on basis of these lines. This is the reason why we do not include the HCN lines in our χ^2 analysis. That said, our overall best fit model is also the model which gives the best fit to the HCN single-dish lines alone and it reproduces the (u, v)-amplitudes nicely. The fits to all four single-dish lines are shown in Fig. 6.5. Only the primary component of the $H^{13}CN$ J=1–0 line is considered when calculating

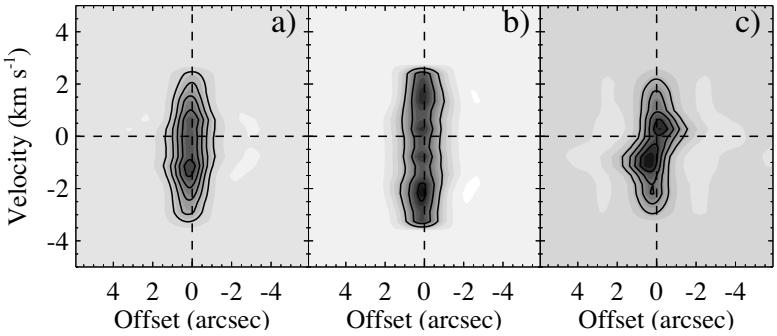

Figure 6.6: Model PV-diagrams of $H^{13}CN$ J = 4–3 at P.A=10°. **a)** Best fit model. **b)** High central mass model with M_*=1.0 $M_\odot$ and α=1.1. **c)** Strongly rotating model with M_*=0.25 and α=0.2. All three panels are directly comparable to the center top panel of Fig. 6.3.

the χ^2. However, our best fit model produces a reasonable fit to the hyperfine components, also for the HCN line.

Figure 6.6 shows the best fit $H^{13}CN$ model PV-diagram (panel a) as well as two other models for comparison, M_*=1.0 $M_\odot$ and α=1.1 (panel b) and M_*=0.25 $M_\odot$ and α=0.2 (panel c). The contour levels in these plots are set to the same values as the levels in Fig. 6.3 and so these plots are directly comparable to the center panel (PA=-10°) of that figure. The best fit model is seen to reproduce the features of the data well in terms of line intensities and emission distribution, while the model in panel b has too weak lines and the model in panel c shows a skewed emission distribution. The asymmetry seen in panel c is typical for a rotating velocity field and this feature is not seen at all in the data. Our best fit model also predicts the HCN J = 4–3 line and this is shown in Fig. 6.7, panel a. Panel b of this figure shows the residual when the model is subtracted from the data (center bottom panel of Fig. 6.3). A strong red-blue infall asymmetry is seen in the model spectra, with the blue peak very much overproduced and a lot of high (negative) velocity material not reproduced by our model. A likely explanation for the overproduction of the HCN emission is that our temperature model is slightly off. Another possibility is that the isotopic abundance ratio is lower than the canonical $^{12}C/^{13}C$ ratio of 70 by 20–30%.

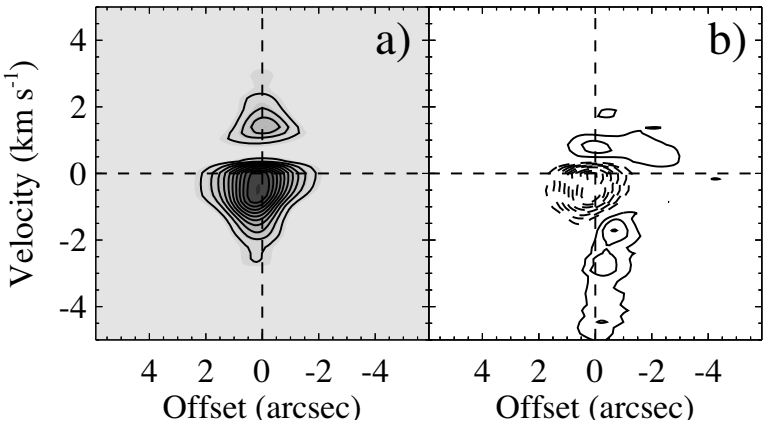

Figure 6.7: Fit to the SMA data of the HCN J = 4–3 line. **a)** shows our best fit model while **b)** shows the residual of the fit. Contour levels are the same as in Fig. 6.3.

6.4.2 Outflow

IRAS2A is known to drive two strong outflows, along axes that are almost perpendicular to each other. We do not model these outflows, and therefore we do not expect to reproduce features in the data that are associated with the outflows. As an optically thin line, we expect that $H^{13}CN$ is much less affected than HCN, and indeed only the single-dish HCN lines show broad wings with excess emission not accounted for by our model. Both the single-dish and the SMA HCN spectra are contaminated by outflow emission, and if we go to the BIMA observations of the low excitation line J = 1–0, it immediately becomes clear that care needs to be taken when modeling the HCN lines. Figure 6.8 shows the BIMA spectrum toward the center of the source. Two models are overplotted, the best fit with a solid line and a model with M_*=1.0 $M_\odot$ using a dashed line style. The observed spectrum is extremely broad with wings extending all the way to ±6 km s^{-1}. Our model does not reproduce these velocities, and indeed, even if we increase the mass significantly, the line width only increases a little.

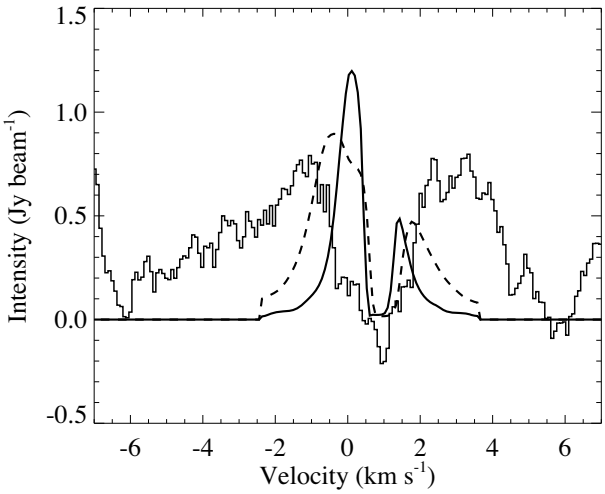

Figure 6.8: A HCN J = 1–0 spectrum toward the center of IRAS2A as observed by BIMA. Two models are overplotted; our best fit model in solid line style and a model with M_*=1.0 $M_\odot$ in dashed line style. The truncation of the model line wings at 2.5 km s^{-1} is due to the finite pixel size of our grid.

6.5 Discussion

We determine the central mass of IRAS2A to be 0.25 $M_\odot$ with an uncertainty of ±0.1 $M_\odot$. This value is considerably smaller than the mass of the envelope of 1.7 $M_\odot$ which is obtained by integrating Eq. 6.1. This makes IRAS2A a true Class 0 object as it falls in the definition of Class 0 where $M_* < M_{\rm env}$. Figure 6.4 shows that our best fit is consistent with a mass accretion rate of 5×10^{-5} $M_\odot$ yr^{-1}. This is a high rate and if the mass accretion rate has been constant, the current central mass would have been accreted in only 5×10^3 yr. However, the accretion rate has probably not been this high in the past or maybe most of the material does not accrete directly onto the star. IRAS2A has a bolometric luminosity estimated to be 20–25 $L_\odot$ and if we assume that this luminosity entirely originates from the accretion through the relation $L = GM_*\dot{M}/r$, the material needs to accrete at a radius of approximately 16–20 solar radii (0.07–0.09 AU), which is about a factor of 6–8 bigger than the estimated stellar radius of young protostars (Stahler 1988) and within the anticipated radius of a disk. From the earlier study of the SMA measurements of the continuum emission, we know that

a compact 0.1 $M_\odot$ component must be present, and this component must also have been built up by the accretion flow within the lifetime of the object. The fact that the material seems to accrete on very small radii suggests that this component is very small and this may explain why we do not see any rotation associated with this component in the data. But does it even make sense to interpret this component as a circumstellar disk given that its mass is almost equal to the stellar mass? One possible explanation of the absence of these velocities is that the disk lies exactly in the plane of the sky and we are viewing it face-on. This however, does not agree with the two outflows which both have components in the plane of the sky and makes it difficult to imagine how a face-on disk would be possible. Another possibility is that the compact component is not really a stable disk (yet?) but rather a pile up of low-angular momentum material very close to the star, which is still dominated by infall. Indeed, Chiang et al. (2008) showed that their high-resolution continuum observations of IRAS2A can be well described without a disk component, when using a magneto-dynamical envelope model rather than a power-law type model like the one used in this work. In any case, it is hard to imagine how a star of 0.25 $M_\odot$ can support such a relatively massive disk in stable rotation. Maybe this material represents the very earliest stages of disk formation? If this is true, given the almost equal mass of star and disk, it implies that the disk begins to form almost simultaneous with the star. It can be argued that it takes of the order of one rotation period to achieve stable rotation (Myers, *priv. comm.*). The rotation period at a radius of the SMA beam ($0.5''$=110 AU) is 2.3×10^3 yr. This is a lower limit because the central mass has most likely been lower in the past, and is comparable to the age derived above. The material may not have made a full rotation and spread out to form a Keplerian disk yet. Using this argument, Keplerian rotation should be detected in a $0.05''$ beam, if the compact density component indeed represents a disk.

We conclude that IRAS2A is an example of a very young protostar based on our best fit velocity model, with both parameters pointing toward a young source. Its velocity field is characterized by a high degree of infall relative to rotation, which in comparison to the study of the velocity field in hydrodynamical simulations of star formation, that was discussed in chapter 3, suggests a young source. In that chapter it was shown that the α parameter evolves smoothly with time from a high value ($\pi/2$) to a low value (0.0) as a core collapses and a disk is formed. A study similar to this one was done in chapter 2 for another young star, L1489 IRS, classified as a Class I source. For this source, a disk was detected based on similar kinematical arguments as we use here, and for that source an α value of 0.26 was found. Based on the value of the α parameter alone, we

conclude that IRAS2A is a younger source than L1489 IRS, and this is entirely consistent with the general perception that Class 0 objects are younger than Class I objects.

6.6 Summary and outlook

In this chapter we have modeled the velocity field of the Class 0 young stellar object NGC1333–IRAS2A. We have constrained our model primarily by the PV-diagram of the $H^{13}CN$ emission observed in very high resolution with the SMA. Despite our high resolution and good signal-to-noise ratio we find no evidence for any rotational motions on any scales, even though a very dense, compact component, interpreted as a disk, is needed on scales of < 100 AU to reproduce the (u, v)-amplitudes, seen in the continuum data.

Repeating this approach for a sample of protostars would allow statistical comparison of the velocity fields of these stars and maybe allow a new evolutionary classification based on α and $M_*/M_{\rm env}$. This will only be possible when the Atacama Large Millimeter Array (ALMA) comes online, because ALMA will be able to do observations like the ones presented here in snapshot mode as opposed to a full night per source needed by the SMA. Furthermore, ALMA will allow us to zoom in on the very centermost parts of protostellar objects and tell us what happens to the velocity field as circumstellar disks form.
In this chapter we did not model the outflow emission that is clearly seen in the BIMA HCN J=1–0 line and also noticeable in the HCN single-dish lines. By using the SMA to observe high-excitation lines, we filter out a lot of the emission on large scale where we expect the outflow to be dominating the velocity field. Still, we do not fit the HCN J=4–3 line very well. This illustrates the need of good radiation transfer outflow models which can be used to investigate the interaction between accretion and outflows on very small scales.

Acknowledgements
The authors would like to thank Ewine van Dishoeck and Phil Myers for useful comments and discussion about the manuscript. CB is partially supported by the European Commission through the FP6 - Marie Curie Early Stage Researcher Training programme. The research of MRH is supported through a VIDI grant from the Netherlands Organization for Scientific Research.

References

Adams, F. C., Shu, F. H., & Lada, C. J. 1988, ApJ, 326, 865

André, P., Ward-Thompson, D., & Barsony, M. 1993, ApJ, 406, 122

Basu, S. 1998, ApJ, 509, 229

Cassen, P. & Moosman, A. 1981, Icarus, 48, 353

Cernis, K. 1990, Ap&SS, 166, 315

Chiang, H.-F., Looney, L. W., Tassis, K., Mundy, L. G., & Mouschovias, T. C. 2008, ApJ, 680, 474

Goodman, A. A., Benson, P. J., Fuller, G. A., & Myers, P. C. 1993, ApJ, 406, 528

Gutermuth, R. A., Myers, P. C., Megeath, S. T., et al. 2008, ApJ, 674, 336

Hogerheijde, M. R. & van der Tak, F. F. S. 2000, A&A, 362, 697

Hogerheijde, M. R., van Dishoeck, E. F., Blake, G. A., & van Langevelde, H. J. 1998, ApJ, 502, 315

Jennings, R. E., Cameron, D. H. M., Cudlip, W., & Hirst, C. J. 1987, MNRAS, 226, 461

Jørgensen, J. K., Bourke, T. L., Myers, P. C., et al. 2007a, ApJ, 659, 479

Jørgensen, J. K., Bourke, T. L., Myers, P. C., et al. 2005a, ApJ, 632, 973

Jørgensen, J. K., Hogerheijde, M. R., van Dishoeck, E. F., Blake, G. A., & Schöier, F. L. 2004a, A&A, 413, 993

Jørgensen, J. K., Johnstone, D., Kirk, H., & Myers, P. C. 2007b, ApJ, 656, 293

Jørgensen, J. K., Schöier, F. L., & van Dishoeck, E. F. 2002, A&A, 389, 908

Jørgensen, J. K., Schöier, F. L., & van Dishoeck, E. F. 2004b, A&A, 416, 603

Jørgensen, J. K., Schöier, F. L., & van Dishoeck, E. F. 2005b, A&A, 435, 177

Lada, C. J. & Wilking, B. A. 1984, ApJ, 287, 610

Looney, L. W., Mundy, L. G., & Welch, W. J. 2000, ApJ, 529, 477

Looney, L. W., Mundy, L. G., & Welch, W. J. 2003, ApJ, 592, 255

Qi, C. 2006, The MIR Cookbook, The Submillimeter Array/Harvard-Smithsonian Center for Astrophysics

Sault, R. J., Teuben, P. J., & Wright, M. C. H. 1995, Astronomical Data Analysis Software and Systems IV, 77, 433

Shu, F. H. 1977, ApJ, 214, 488

Stahler, S. W. 1988, ApJ, 332, 804

Terebey, S., Shu, F. H., & Cassen, P. 1984, ApJ, 286, 529

Ward-Thompson, D. & Buckley, H. D. 2001, MNRAS, 327, 955